Visualising Co nanoparticle aggregation and encapsulation in Co/TiO2 catalysts and its mitigation through surfactant residues

Chengwu Qiu [a,b], Yaroslav Odarchenko [a,b], Ines Lezcano-Gonzalez [a,b], Qingwei Meng [c], Tom Slater [d], Shaojun Xu [b,d], Andrew M. Beale [a,b,*]

[a] Department of Chemistry, University College London, 20 Gordon Street, London, WC1H 0AJ, UK
[b] Research Complex at Harwell (RCaH), Harwell, Didcot, Oxfordshire, OX11 0FA, UK
[c] School of Chemical Engineering and Light Industry, Guangdong University of Technology, Guangzhou 510006, China
[d] Cardiff Catalysis Institute, School of Chemistry, Cardiff University, Cardiff, CF10 3AT, UK

ARTICLE INFO

ABSTRACT

Due to the reducible nature of TiO_2, the encapsulation of cobalt nanoparticles (CoNPs) by reduced TiO_{2-x} is often reported to decrease their catalytic performance in reactions such as Fisher-Tropsch synthesis (FTS). Here, we show using HAADF-STEM imaging and electron energy loss spectroscopy (EELS) that a residual $C_{12}E_4$ surfactant used to prepare the CoNPs, remains on the surface of a TiO_2 rutile support, preventing the formation of Ti^{3+}/Ti^{2+} oxides and therefore TiO_{2-x} migration. Furthermore, the presence of these surfactant residues prevents the coalescence and aggregation of CoNPs during catalyst preparation, maintaining the dispersion of CoNPs. As such, using $C_{12}E_4$ in the preparation of Co/TiO_2 can be considered beneficial for producing a catalyst with a greater number of active Co species.

© 2023 The Author(s). Published by Elsevier Inc. This is an open access article under the CC BY license (http://creativecommons.org/licenses/by/4.0/).

1. Introduction

A support, when used in heterogenous catalysis, is there primarily as a delivery medium of the active component often in the form of atoms, clusters or nanoparticles. More importantly, the interaction between the two can be optimised to improve dispersion, stability, tunability of the active component and even in some cases play a critical role in the catalytic process. The supports typically comprise both oxides (e.g. SiO_2, TiO_2, Al_2O_3, CeO_2, and zeolite) [1–3] and carbides (e.g. carbon and SiC) [4,5]. Among those, TiO_2-supported, cobalt nanoparticles (CoNPs) are widely reported in literature. [1,6,7,8,9,10,11] However, there is a big challenge to produce a Co/TiO_2 catalyst with desired performances since CoNPs often end-up encapsulated by reduced amorphous TiO_{2-x}. [8,9,10,11] This problem leads to the blockage of the active surface and is therefore inimical to the catalyst activity [8,10]. Encapsulation shows a dependency with TiO_2 polymorph [12–14], with anatase, typically possessing a high concentration of defects, being more susceptible to this phenomenon than rutile

[12,14]. An additional problem concerns the formation of metal-support compounds such as the non-reducible cobalt titanate, [15–17] leading to a loss of the active metallic cobalt for reactions. The mobility of Co and, in particular, the spreading of cobalt on the titania surface [18–20] exacerbates the formation of such titanate compounds. Fortunately, even this titanate formation can be mitigated against by the addition of small amounts of noble metals [21]. However, Melaet et al. [11] reported that cobalt oxide (CoO_x) can form a unique interface with TiO_2, which was more active than metallic Co/TiO_2 for Fisher-Tropsch synthesis and CO_2 hydrogenation. The above precis suggests that there is value in expending time and effort to mitigate encapsulation by TiO_{2-x} to develop better performing catalysts. Approaches for mitigating encapsulation include the application of a post-treatment reduction–oxidation-reduction (ROR) cycle to break and disperse the amorphous TiO_{2-x} layer [10]. An alternative strategy would be to inhibit the formation of TiO_{2-x} in the catalyst in the first place. Indeed, Hong, et al. [22] recently reported a novel approach applying a carbon nitride (C_3N_4) coating onto TiO_2 before adding the CoNPs, which subsequently showed improved FTS stability by stopping both CoNP agglomeration and encapsulation. A similar approach was adopted by Phaahlamohlaka, et al., but this time using mesoporous silica to obtain the sintering-resistant Co catalysts, although they did not

---

* Corresponding author.
E-mail address: Andrew.Beale@ucl.ac.uk (A.M. Beale).

report whether the silica coating also inhibited the formation of a TiO_{2-x} layer [23].

The size of nanoparticles is another important parameter in catalytic research. For example, for FTS activity a typical critical size of CoNPs is determined to be 5–10 nm, [24–27] although no dependency on CoNP size is shown when the critical size is exceeded (i.e. > 10 nm) while below this, the activity shows a linear relationship with CoNP size. The size effects also affect the product selectivity [24,28,29] and nanoparticle stability [30,31]. The reasons for these nanoparticle size effects are not clear, but could be related to the size-dependent active sites contain more uncoordinated atoms but less B5 active sites in small NPs lead to adsorbates that are harder to remove [25,26,32]. In order to control the size of CoNPs (5–10 nm), various methods have been successfully employed, including for example, pre-synthesizing size-controllable NPs using reverse micelles [33–35], thermal decomposition [36], using organic solvents in place of water during impregnation [26,37], and modification of the support surface [38].

Here we report an alternative synthetic approach to mitigate CoNP aggregation and encapsulation, using a $C_{12}E_4$ surfactant. We demonstrate the impact of the $C_{12}E_4$ surfactant by preparing two similar catalysts, differing only in the point at which removal of the surfactant occurs; the early removal of the surfactant leading to aggregation of the CoNPs during preparation. We note that a similar 'protective surfactant' strategy has been successfully employed to prepare other types of catalysts, including a sintering-resistant Au/TiO_2 catalyst for CO oxidation [39,40]. In that work, the authors observed that a polydopamine / oleylamine layer stops Au migration, preventing sintering via Ostwald ripening during calcination due to the formation of a strong metal-support interaction, with thermal decomposition of the surfactant leading to the formation of a protective carbon layer. Although this carbon layer can be removed by calcination, the strong interaction between Au and TiO_2 is maintained, ensuring a high Au dispersion which allows for optimal CO oxidation. A di-block poly(styrene)-*block*-poly(2-vinylpyridine) polymer is also widely reported to obtain uniform nanoparticle size although it is very expensive [41–43]. Due to the repulsion of ploy-styrene block in a reverse micelle, the nanoparticles can be individually maintained before and after depositing on a support. In contrast, our work here focused on the effect of surfactant on aggregation of CoNPs before calcination, reducibility of CoNPs and TiO_2 support during reduction, as well as improvement in CO reduction reaction *without* the formation of a carbon layer. The complex-like $C_{12}E_4$ derivatives formed during preparation coat the surface of size-controllable CoNPs and the titania support, which has a shielding effect that protects TiO_2 from being reduced and decorating the CoNPs. Even though the reducibility of the catalyst is lower, CO reduction is significantly enhanced.

2. Results and discussion

2.1. Identifying surfactant residues and determining their effect on the properties of the supported cobalt nanoparticles

Two types of catalysts were prepared using reverse micelle encapsulation. The first type of catalyst, labelled 5–15 %Co, contains 5–15 % wt. Co on TiO_2 deposited via inverse micelles and subsequently treated with acetone to break the micelles and remove surfactant. In the second type, 5–15 %Co@$C_{12}E_4$, since no acetone wash was performed, the micelle remains intact. The textural properties of calcined samples are found in Table S1, where a significant lower surface area is seen in 15 %Co due to the blockage by large amounts of surfactant residues.

Calcination at 473 K in air of both samples should see the decomposition of the $Co(OH)_2$ precipitate to form Co_3O_4 [33,44]. However, possibly due to the low temperature used for calcination, decomposition is incomplete (Fig. 1a) with both $Co(OH)_2$ and Co_3O_4 observed to be present [45]. The sample was then subjected to reduction for 3 h at 623 K in 50 % H_2/He which saw the reduction of $Co(OH)_2$ and Co_3O_4 to Co fcc (Fig. 1b). Fig. 2 shows the Fourier Transform Infrared Spectra (FTIR) of the heat-treated catalysts. In the calcined samples, there are bands present at 1120, 1724 and ~ 2900 cm^{-1} due to C—O, C=O and CH_2/CH_3 stretching modes, which are suggestive of the formation of the polymer-like species formed via ester polymerisation in the unwashed catalysts (5–15 %Co@$C_{12}E_4$). Two bands can be assigned to C=O (1724 cm^{-1}) and COO$^-$ (1590 cm^{-1}), respectively, and are more intense in the 15 %Co@$C_{12}E_4$ than in the 5 %Co@$C_{12}E_4$ sample [46]. Koizumi, et al. observed the same functional group formation from various glycol-containing compounds and proposed the formation of polymer-like complex species *via* ester polymerization during calcination at 400 K [46]. Hence, similar polymeric species are considered to be present in these samples after calcination or heating in H_2. The presence of IR bands due to C=O, suggests that cross-linking has taken place to produce a polymer in addition to some residual surfactant; the presence of residual micelle can be seen particularly in the parts of the spectra where the C—O/CH stretches occur. Unsurprisingly, the unwashed catalysts, particularly the 15 %Co@$C_{12}E_4$, contain a large quantity of surfactant residues (~50 %, estimated from the TGA data shown in Fig. S2a). Note also the presence of a sharp band at 1384 cm^{-1} in the 5–15 %Co catalysts due to residual nitrate [47]. It is thought that this nitrate remains encapsulated into the CoNPs in the washed catalysts and cannot be fully decomposed using the mild calcination conditions employed.

Fig. 3 & Figure S2 shows Thermal Gravimetric Analysis (TGA) data containing mass loss profiles for samples 5–15 %Co@$C_{12}E_4$ and 5–15 %Co after calcination and after reduction for 3 h at 623 K in 50 % H_2/He. The weight loss occurring in all samples before 400 K is due to the loss of adsorbed water. For the calcined samples, the first derivative peaks after 600 K can be attributed to the decomposition of remaining $C_{12}E_4$ derivatives (Fig. 3b & S2b) whereas the weight losses after 1000 K comprise contributions derived from the reduction of cobalt oxide (i.e. $Co_3O_4 \rightarrow CoO$). These TGA data also confirm therefore that residual $C_{12}E_4$ surfactant breaks down to yield polymeric compounds during calcination. For example, in Fig. 3b, the mass loss finished at ~ 642 K in pure $C_{12}E_4$ and in the physical mixture of rutile + $C_{12}E_4$, whilst in the calcined rutile + $C_{12}E_4$ mixture or 5–15 %Co@$C_{12}E_4$ samples, the mass loss continues beyond this temperature [46].

In contrast, for the samples that had undergone the reduction treatment the weight loss is minimal, indicating that only a very small amount of the surfactant remained on the sample. We estimate that ~ 95 wt% of the surfactant is removed after reduction for the 5 %Co@$C_{12}E_4$ sample (see Fig. 3a). This is also confirmed from analysis of the mass spectrometry (MS) traces in Figure S3, which show that significant mass loss of hydrocarbon species occurs between 50 and 100 min during the reduction treatment.

We propose that in samples that have not been subjected to reduction at elevated temperatures, the deposits remaining on the 5–15 %Co@$C_{12}E_4$ surface would present some barrier between H_2 and the Co species preventing sample reduction (*vide infra*). Acetone washing however, removes the $C_{12}E_4$ compound in the sample (only ~ 1 % remains in the fresh 5 %Co sample, according to Fig. 3a) enabling more facile cobalt oxide reduction. Increasing Co loading (15 %Co) leads to residual surfactant encapsulation in the aggregated CoNPs and is proposed to be the cause of the strong derivative peak at 513 and 701 K in Figure S2b; the first peak is thought to be the decomposition of residual α-Co(OH)2 (in addi-
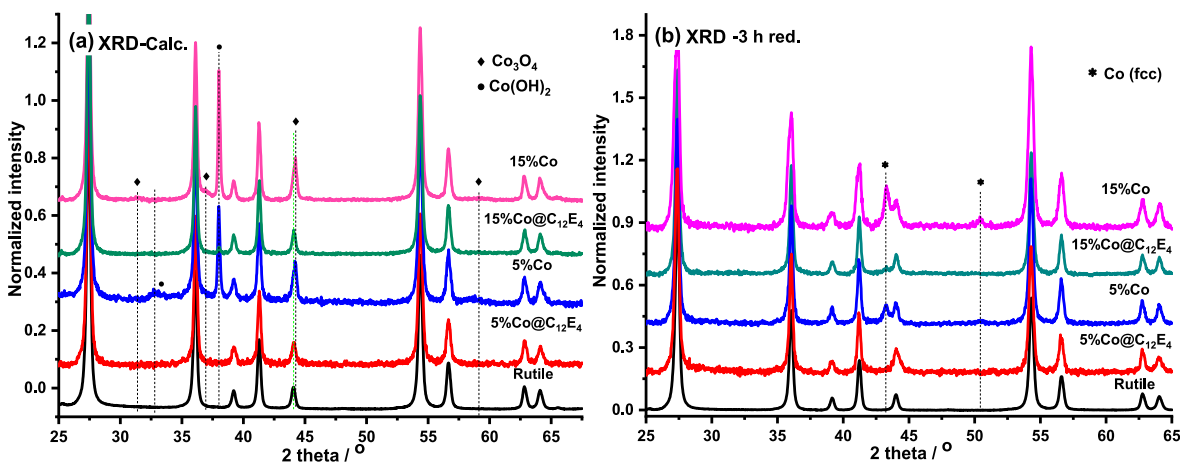
Fig. 1. XRD patterns of 5–15 %Co@$C_{12}E_4$ and 5–15 %Co catalyst before (a) and after (b) reduction at 623 K in 50 % H_2/He for 3 h. Note that for the samples where the micelle was removed before calcination (a) Co(OH)$_2$ and Co_3O_4 is detected whereas after reduction (b) the Co-fcc phase is observed.
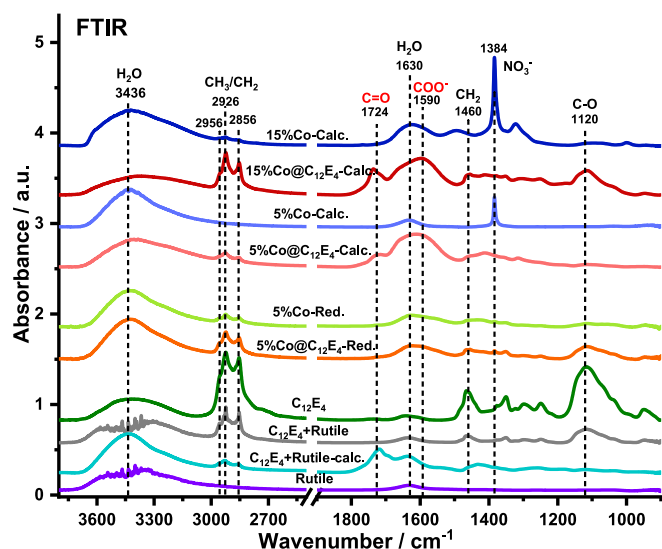
Fig. 2. Reference FTIR spectra for the components used to prepare the catalysts, plus those obtained from samples 5–15 %Co@$C_{12}E_4$ and 5–15 %Co after calcination and reduction. The unique absorption band at 1724 cm^{-1} for 473 K calcined catalysts demonstrates the formation of complex-like $C_{12}E_4$ derivatives. Reduction in H_2 at 623 K for 3 h removes these compounds. Note, the band at 1384 cm^{-1} disappears in 5 %Co after reduction, indicating decomposition of residual nitrate salt. For the reduced samples, the absorption at ∼ 2900 and 1120 cm^{-1} is mainly attributed to residual ethanol, which is used for isolation of reduced cobalt from air.

tion to decomposition of residual nitrate salt – see the MS response at m/z 28 & 46 after ∼ 30 min in Figure S3f), while the second peak at 701 K is attributable to removal of the residual surfactant.

It is assumed that the initial CoNP size in all samples is broadly similar, since the same one-pot cobalt-micelle solution was used to prepare them. On close inspection of Fig. 4, the mean CoNP size in 5 %Co (10 nm) and 15 %Co (13 nm) is a little larger than that seen for the 5 %Co@$C_{12}E_4$ (8 nm) and 15 %Co@$C_{12}E_4$ (9 nm). We attribute the greater particle size seen in the former samples due to the addition of acetone which can break the micelles leading to movement of the Co species and partial aggregation of the CoNPs (Figure S4b). Interestingly, where a Scherrer analysis can be performed on the data shown earlier in Fig. 1b, there is a good correlation with the mean particle size as determined from the Transmission Electron Microscopy (TEM) images (∼17 nm of metal CoNPs for 15 %Co, ∼ 11 nm for 5 %Co, ∼ 10 nm for 15 %Co@$C_{12}E_4$,

∼ 9 nm for 5 %Co@$C_{12}E_4$). Furthermore, there is consistency in the observation that for samples 5–15 %Co the reflections appear narrower and indicative of larger crystallites (Fig. 1) compared to samples 5–15 %Co@$C_{12}E_4$.

The reducibility of the cobalt species and the samples in general was determined using H_2-TPR (in 10 % H_2/N_2) and shown in Fig. 5a. In the 5 %Co, there are two groups of H_2 consumption peaks before and after 700 K, corresponding to the reduction of Co_3O_4 and Co(OH)$_2$ to Co^0 and CoTiO$_3$ to Co^0, respectively [15,48,49,50]. Increasing cobalt loading to 15 wt% (15 %Co), sees significant differences in the reduction behaviour. Firstly, there is a small but unique double-peak before 560 K (∼9 % relative to all the H_2-TPR peak area), which is equivalent to the TPR profile of unsupported CoNPs (Co_3O_4),[51,52] indicating the presence of aggregated CoNPs in this sample that are not strongly interacting with the TiO_2 support (see Fig. 5a insert). Additionally, a small bump (see *) just below 500 K in 5 %Co is seen and may be due to the aggregated NPs, but it contributes less to the signal (∼5 % of signal intensity). The main consumption of H_2 for the 15 %Co sample in Fig. 5a comprises overlapping responses, corresponding to the delayed reduction of Co_3O_4 + Co(OH)$_2$ → Co^0. [49,50] CoTiO$_3$ formation and reduction to Co^0 is minimal in this sample based on the negligible H_2 consumption over 800 K, which indicates a weak interaction between cobalt and titania [53]. In contrast, the 5–15 %Co@$C_{12}E_4$ samples are difficult to reduce with only minor H_2 consumption observed at temperatures below 673 K and only two major peaks (corresponding to Co_3O_4/Co(OH)$_2$ and CoTiO$_3$ reduction to Co^0) present in those samples above this temperature. This can be attributed to the effect of covering of the Co nanoparticles by the surfactant and/or the smaller NP size in the samples. Initially, the reduction of 5 %Co@$C_{12}E_{4x}$ seems easier than the 15 %Co@$C_{12}E_4$ (see the high proportion of the H_2 consumption before 623 K in Fig. 5a, namely ∼ 8.2 % for 5 %Co@$C_{12}E_4$ while only ∼ 2.2 % for 15 %Co@C_{12}-E_4). This could be due to the higher weight of surfactant coverage in 15 %Co@$C_{12}E_4$ (see Figure S2) and indeed support for this proposal can be seen in the form of the negative TCD response at 715 K that is thought to be due to the decomposition of the surfactant [54]. However, the second peak in 5 %Co@$C_{12}E_4$ centred at 845 K is higher than the peak seen in 15 %Co (810 K). It is proposed that a higher proportion of CoNPs in the 5 %Co@$C_{12}E_4$ sample are in contact with the titania surface than for the 15 %Co@$C_{12}E_4$ sample. This would then lead to more cobalt titanate (CoTiO$_3$) species, which are known to be more difficult to reduce than the cobalt oxides [15,48].
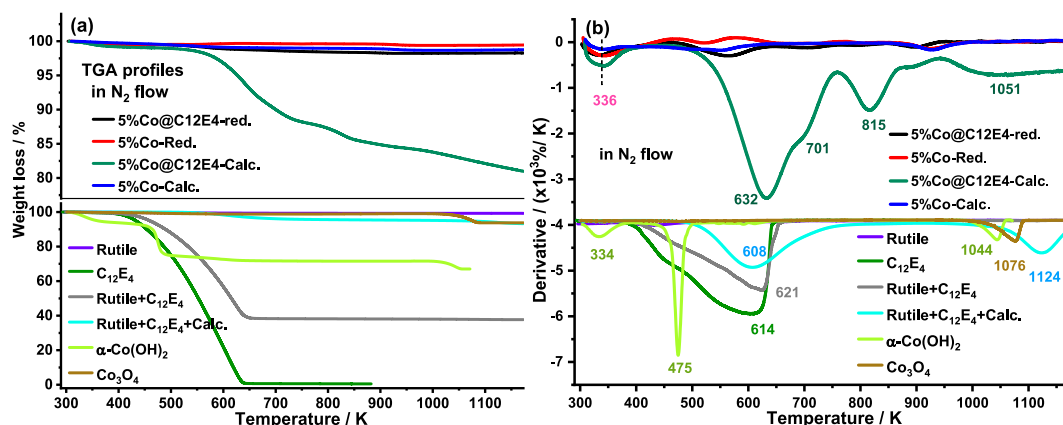
Fig. 3. TGA (a) and the corresponding first derivative (b) profiles of 5%Co@$C_{12}E_4$ and 5%Co catalysts with and without reduction.
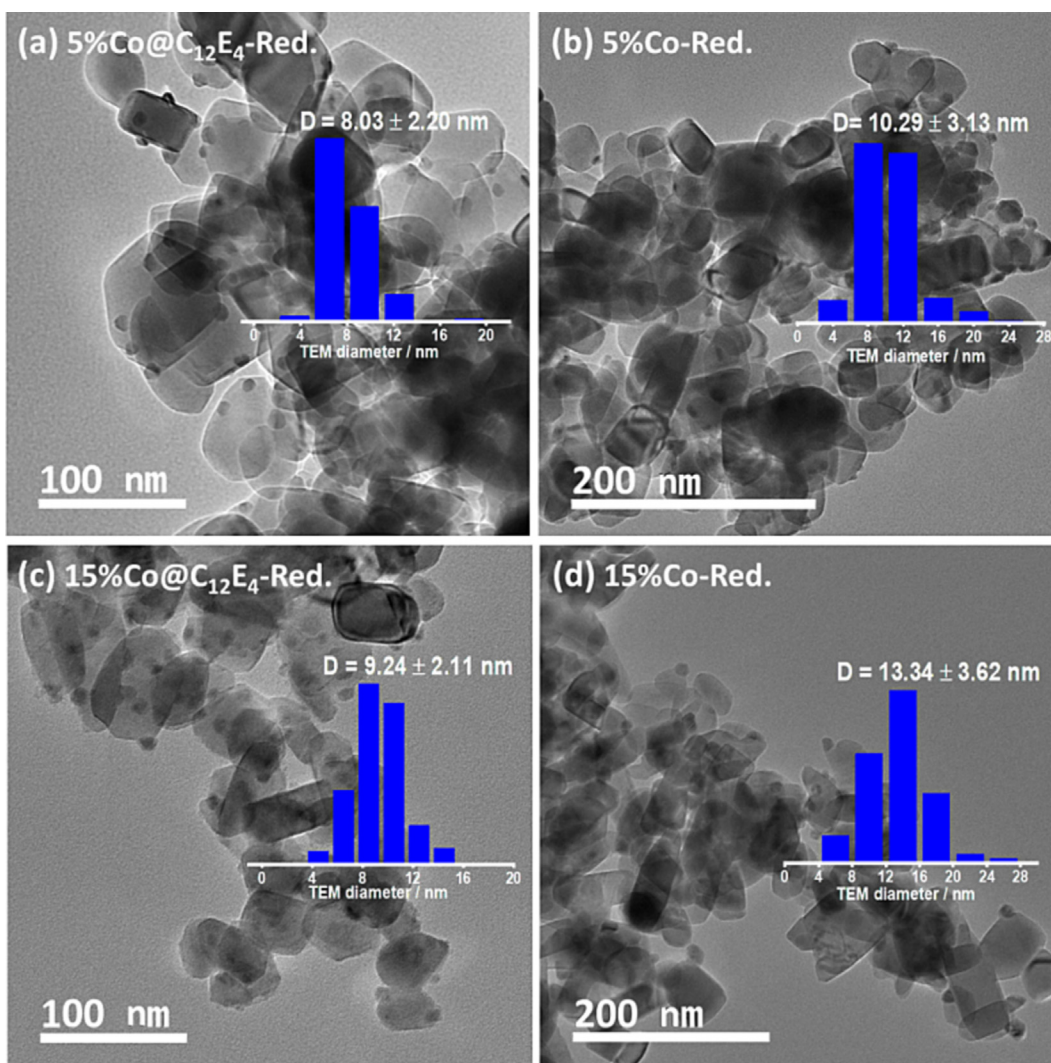

Fig. 4. TEM images and corresponding histograms of nanoparticle size distributions for 5–15 wt% Co loaded catalysts after reduction at 623 K in 50 % H_2/He for 3 h. The observed number of individual NPs is lower in the 5–15 %Co than in the 5–15 %Co@$C_{12}E_4$ catalysts, although the initial Co loading was the same.

The Degree of Reduction (DOR) of the samples is calculated based on their isothermal H_2-TPR (Fig. 5b). After 3 h at 623 K in 10 % H_2/N_2, the DOR values are: 45.7 % for 5 %Co@$C_{12}E_4$, 69.1 % for 5 %Co, 55.4 % for 15 %Co@$C_{12}E_4$ and 85.2 % for 15 %Co respectively. A slower decrease in H_2 consumption is observed for the

5–15 %Co@$C_{12}E_4$ samples during the isothermal period (at 623 K, particularly a jump centred at 90 min in 15 %Co@$C_{12}E_4$ in Fig. 5b), while H_2 consumption decays rapidly in the 5–15 %Co samples (e.g. TCD response from 38 to 0 within 45 min for 15 % Co, Fig. 5b). Hence the reduction process occurs to a significant
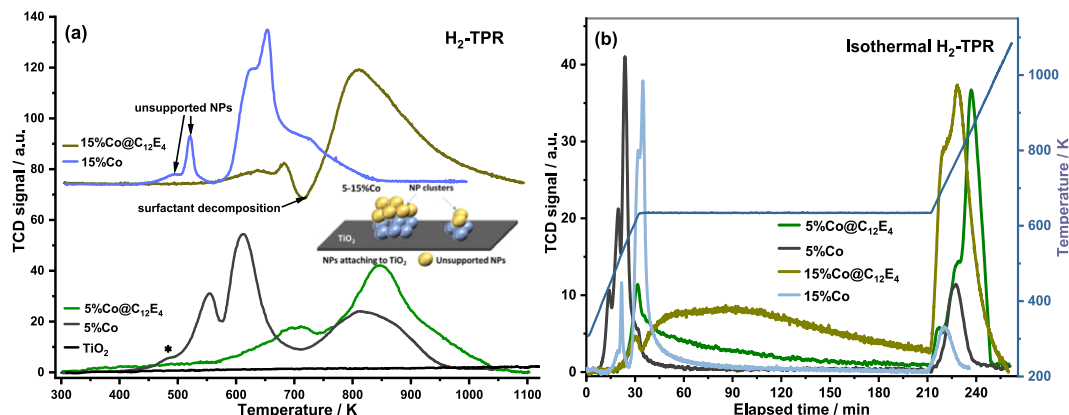
Fig. 5. H$_2$-TPR using a ramp rate of 10 K/min (a) and isothermal-H$_2$-TPR at 623 K for 3 h (b) profiles for cobalt catalysts heated in 10 % H$_2$/N$_2$ (50 mL/min).

extent during isothermal treatment for the 5–15 %Co@C$_{12}$E$_4$ catalysts, while it is negligible for the acetone-washed ones. As mentioned before, residual surfactant can be almost completely decomposed and removed after the 3 h reduction process, so the dominant factor affecting the DOR for 5–15 %Co@C$_{12}$E$_4$ would be the coverage of surfactant residue in the early stages of reduction (<1 h, including ramping) and the cobalt-titania interaction in the latter stages (after 1 h reduction). In contrast, for 5–15 %Co, the lack of surfactant residues renders the cobalt-titania interaction more noticeable.

### 2.2. Visualising the Cobalt-Rutile interface

HAADF-STEM images for the samples 5 %Co@C$_{12}$E$_4$ and 5 %Co after reduction for 3 h at 623 K are shown in Fig. 6 a and b, and corresponding Electron Energy Loss Spectra (EELS) are shown in Fig. 6 c and d. The combined STEM/EELS is an insightful technique that allows us to obtain chemical and structural information with high (nm) spatial resolution [55]. From the STEM images, a single CoNP bound to the titania support is clearly observed and from this we can define sub-regions (red squares), labelled respectively from 1 to 8 in Fig. 6 a and b, from where EELS spectra were recorded in order to determine the local Ti and Co species. Only Ti^{4+} is detected in the 5 %Co@C$_{12}$E$_4$ sample in region 1 (Fig. 6a) which comprises the TiO$_2$ support, while in the corresponding 5 %Co sample, Ti^{3+} is the main component (see Table S2a for details of the Linear Combination Fitting (LCF)) in region 1 of Fig. 6b. Note the nature of the TiO$_2$ environment (crystalline or non-crystalline) cannot simply be concluded from the visibility of lattice planes in Fig. 6a, b, as this is mainly caused by the orientation of the crystalline domains to the electron beam. Interestingly, both Ti^{3+} and Ti^{2+} are detected at the cobalt-titania interface in both samples (region 2 and Table S2a), although in the 5 %Co@C$_{12}$E$_4$ sample Ti^{4+} is present in minor amounts (~11 % Table S2a) at this interface. This localised reduction can be explained as an effect of the metallic cobalt promoting TiO$_2$ reduction to Ti$_2$O$_3$ or even to TiO via a H$_2$ spillover effect [56]. The more reduced TiO$_2$ in 5 %Co is also evidenced by a respective blue-shift of the Co 2p and red-shift of Ti 2p peaks in the XPS spectra shown in Figure S7.

Similarly, from the EELS spectra in Fig. 6d for the cobalt component, differences in composition can be observed, as determined from LCF analysis (with the results shown in Table S2b). As determined from the above TPR data, less metallic cobalt is determined to be present in the 5 %Co@C$_{12}$E$_4$ (~40 %) than in 5 %Co (~60 %). More specifically, regions 2 & 3 in the NP shown in Fig. 6 a & b contain 67 vs 89 and 9 vs 74 % metallic cobalt (Table S2b). The lower quantity of metallic cobalt in region 3 of 5 %Co@C$_{12}$E$_4$ is likely due

to surface oxidation during passivation (a flatter NP with a similar CoO$_x$ layer is observed in Fig. 6b) while the low metal content at the interface (region 2) could be due to the strong interaction with TiO$_2$. The NPs featured in the two samples and depicted in Fig. 6 a & b are similar in width (~13 nm) and height (5–7 nm) and therefore under normal circumstances the DOR for both NPs would be expected to be similar. The fact that they are not, can be ascribed to the effect of the residual C$_{12}$E$_4$ surfactant (see Fig. 3). It not only suppresses cobalt oxide reduction but also inhibits H$_2$ spillover from cobalt to titania and therefore leads to a lower degree of TiO$_2$ reduction.

EELS spectra in several other regions of Fig. 6 a, b were also acquired and analysed. In regions 6 and 7 of Fig. 6a and regions 3–5 and 7 of Fig. 6b, Ti^{3+}/Ti^{2+} species are also detected (Figure S5) although the spectra are noisy. However, no Ti species are seen in regions 3–5 of Fig. 6a and region 6 of Fig. 6b. Analysis of the elemental maps (Fig. 6 a1-a3 and b1-b3) also reveals no Ti on the surface of the CoNP. These observations contrast with findings in the literature where it has been reported that reduced TiO$_{2-x}$ often forms a layer several nanometres thick to fully cover metal NPs [57–59]. Here, Ti^{3+}/Ti^{2+} migration leads to decoration of the periphery of NPs at the interface with the support in both samples. This difference could be in part due to the use of the more stable rutile polymorph as opposed to the more common P25 or anatase [12]. It is clear that the decoration of Ti^{3+} in 5 %Co occurs to a greater extent than in 5 %Co@C$_{12}$E$_4$ with a high degree of TiO$_2$ reduction to Ti$_2$O$_3$/TiO confirmed in Fig. 6c and Table S2a.

A further examination of the cobalt-titania interaction in the two samples (but from different regions to Fig. 6) was also performed via analysis of the Fast Fourier Transform (FFT) patterns extracted from HAADF-STEM images (Fig. 7). The support of 5 % Co@C$_{12}$E$_4$ (region 4 in Fig. 7a) displays a rutile TiO$_2$ structure (d-spacing 1.7 Å / {2 1 1} planes) and again the FFT patterns show no evidence of (crystalline) TiO$_{2-x}$ on the CoNPs (regions 1 ~ 3, 5); note however that in Fig. 6a, Ti^{3+}/Ti^{2+} species are seen at the periphery of the NPs (see EELS spectra in region 6, 7, Figure S5a). However, for 5 %Co in Fig. 7b a corundum Ti$_2$O$_3$ structure (region 4 in Fig. 7b) is determined from the FFT patterns (d-spacing 2.7 Å / {10 -1 4}, 2.2 Å / {2 -1 13}). Note that Ti$_2$O$_3$ is seen at the periphery of the CoNP in Fig. 7b, while it is not detected in similar profiled regions (2 & 5) of Fig. 7a for the 5 %Co@C$_{12}$E$_4$ sample. Further evidence of Ti$_2$O$_3$ migration to the surface of CoNPs can be seen from the FFT patterns (region 2 of Fig. 7b). The crystal phases of cobalt present in both samples are determined to be either cobalt oxide or metallic cobalt, although the latter is present in lower quantities in 5 %Co@C$_{12}$E$_4$ (Fig. 7a) than 5 %Co (Fig. 7b). This is in line with the linear combination fitting results of EELS cobalt spectra in
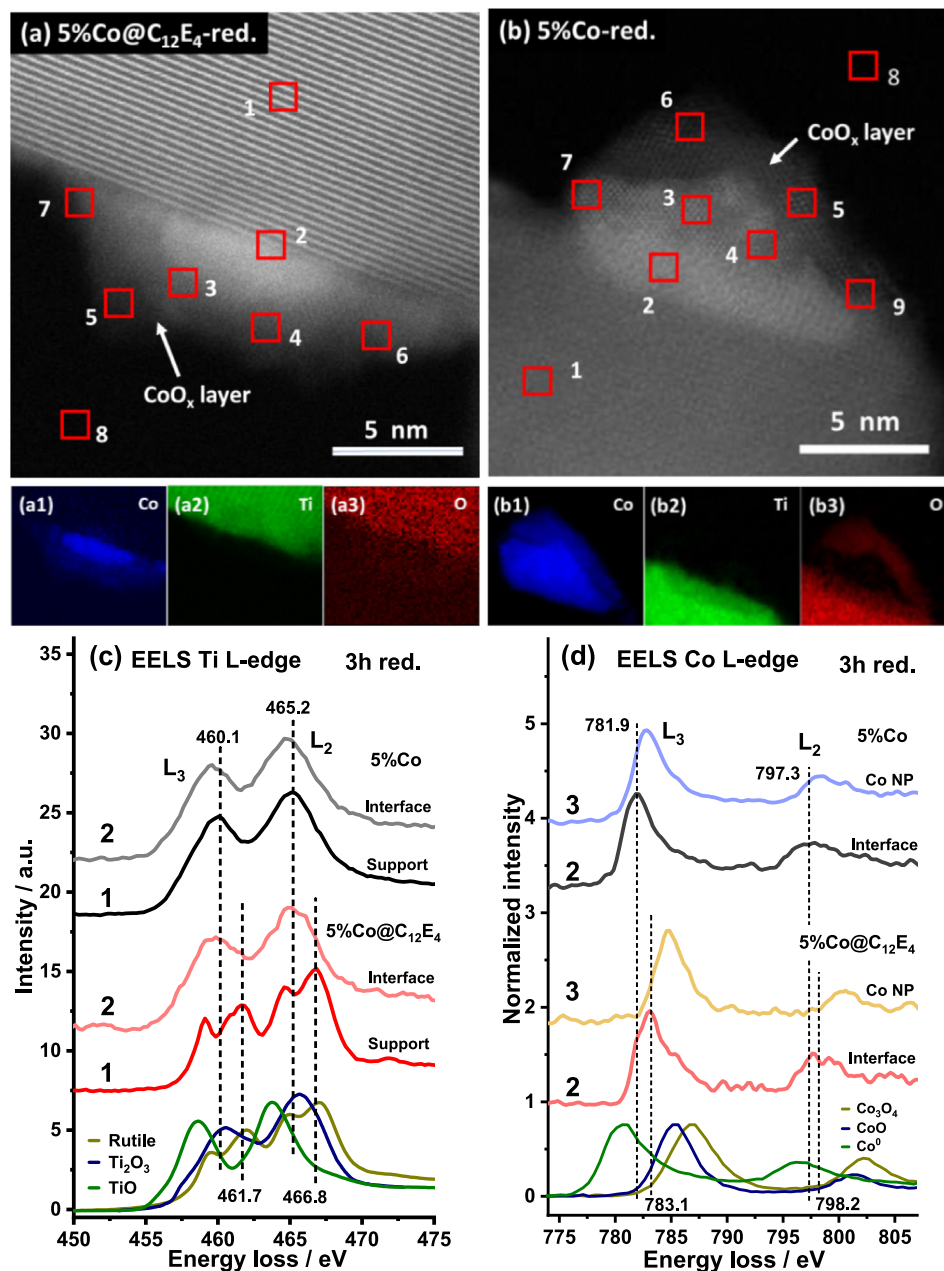
Fig. 6. (a, b) HAADF-STEM images and EELS elemental maps (a1-a3; b1-b3) of the reduced catalysts (3 h, 623 K) with corresponding single point L-edge EELS spectra shown for Ti (c) and Co (d) respectively. The reduced catalysts were passivated with 1 % O_2/He at 303 K for 30 min, hence the presence of a CoO_x layer on the CoNPs.

Table S2b and DOR values from TPR in Fig. 5, and partially due to the NPs being more highly dispersed. The presence of more reduced Co in 5 %Co sample also suggests the TiO_{2-x} layer to be crystalline, which can inhibit gas diffusion [58,60] and protect the reduced cobalt from oxidation during passivation. In contrast, the TiO_{2-x} in 5 %Co@$C_{12}E_4$ is amorphous and permeable, allowing the contact between gas molecules and NPs and which we propose allows for oxidation of NPs during passivation [58,60]. We propose that the presence of highly dispersed cobalt and low prevalence of Ti^{3+}/Ti^{2+} in 5 %Co@$C_{12}E_4$ are both attributable to the effects of surfactant residues present after calcination.

2.3. Rationalising the differences in CO conversion

A summary of the CO reduction performance of the two types of catalyst under ambient conditions (493 K, H_2/CO = 2, 1 bar) are given in Table S3; note the low conversions obtained allow us com-

pare the catalytic performance. As can be seen in the table, although the CO conversions drop with time, it is clear that the Cobalt Time Yield/Turnover Frequenceis (CTY/TOFs) in 5 %Co@C_{12}-E_4 are observed to be $\sim$ 4 times higher than in 5 %Co throughout the reaction. A tripling of the cobalt loading to 15 wt% leads to a narrowing of the activity gap (the 15 %Co@$C_{12}E_4$ CTY/TOFs are only $\sim$ 2 times greater than the 15 %Co sample). When comparing the effects of reduction time, it is noteworthy that the 5 %Co@$C_{12}E_4$ samples show improved CTY/TOFs with increased reduction time whereas the 5 %Co samples exhibited a worsening in performance. Based on these data it is possible to identify the differences in performance to be due to the amount of active component (i.e. DOR), CoNP size and morphology, etc. The DOR value reflects the amount of metallic cobalt (fcc) present; the component which is considered active and responsible for CO conversion (i.e. 5–15 %Co@$C_{12}E_4$ samples < 55 % vs 5–15 %Co samples > 69 % reduction). We note however, that in Co/TiO_2 catalysts it has been reported that the
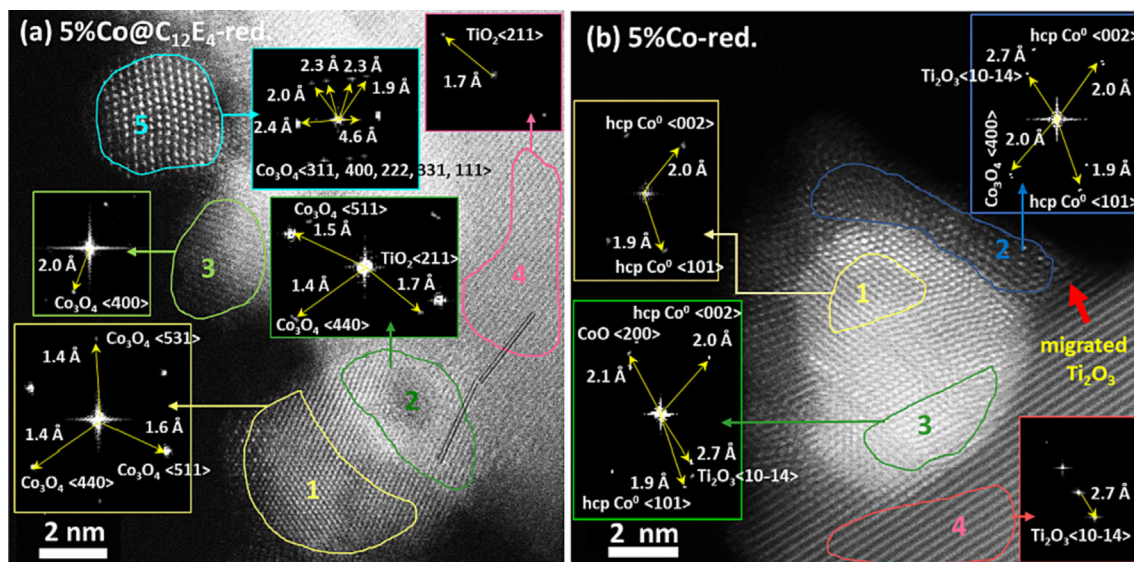
Fig. 7. HAADF-STEM images of the reduced catalysts and their corresponding fast Fourier transform patterns in marked regions for (a) 5 %Co@$C_{12}E_4$-red and (b) 5 %Co-red. The reduced catalysts were passivated with 303 K 1 % O_2/He for 30 min before being imaged. In (a) Co_3O_4 is present in regions 1, 3, 5; whilst TiO_2 is the sole component in region 4, whilst region 2 contains a mixture of these oxides. In (b) Co^0 is seen in region 1; Ti_2O_3 in region 4, and mixture of Co^0, CoO/Co_3O_4 and Ti_2O_3 in regions 2 and 3. Note changes in the Co or TiO_2 lattice-spacing caused by the metal-support interaction were not detected. (For interpretation of the references to colour in this figure legend, the reader is referred to the web version of this article.)

interface between the Co NPs and TiO_2 is more active, than the Co NPs themselves [11]. We propose therefore that the 5–15 % Co@$C_{12}E_4$ catalysts possesses a larger CoO_x-TiO_2 interface than the 5–15 %Co samples and hence are both more difficult to reduce whilst being more active [11]. When considering the effect of CoNP size in isolation, the larger crystallite sizes (10 and 13 nm respectively) observed in 5–15 %Co catalysts indicate that the active surface area for CO conversion should be lower in these samples than those seen in 5–15 %Co@$C_{12}E_4$ (8–9 nm). Note that differences in intrinsic CO reduction activity should be ignored, as the average NP size is above the critical size range (5–10 nm) reported in literature [24,26]. Another principal cause for lower performance in our TiO_2 supported catalysts is due to a manifestation of the strong metal support interaction (SMSI) effect leading to Co NP decoration with Ti^{3+}/Ti^{2+} species [61,62]. According to the HAADF-STEM images shown in Fig. 7, the sub-oxides TiO_{2-x} observed on 5 %Co are crystalline and likely impermeable, blocking the contact between syngas and NPs. The presence of $C_{12}E_4$ derivatives (polymers) on the 5–15 %Co@$C_{12}E_4$ catalysts appears to prevent TiO_2 from being reduced to TiO_{2-x} and migrating onto the CoNPs, thereby leaving a clean and open surface for CO reduction; this according to TGA which suggested reduction removes all $C_{12}E_4$ and their derivatives. Therefore, these data indicate that surfactant-coated catalysts can exhibit better CO reduction performance. Indeed, from Table S3, the surfactant coated 5–15 % Co@$C_{12}E_4$ catalysts exhibit a greater TOF during an ambient pressure CO reduction test. This indicates a combination of smaller NP size, lower degree of CoNP aggregation and extent of Ti^{3+}/Ti^{2+} coverage accounts for the differences in performance in surfactant coated 5–15 %Co@$C_{12}E_4$ samples.

3. Summary and conclusion

The purpose of this work is to demonstrate how residual $C_{12}E_4$ surfactant used in catalyst preparation can prevent both CoNP aggregation during preparation and TiO_2 reduction and migration during pre-reduction treatment. Although coverage by TiO_{2-x} species of the CoNPs occurs to some extent in both samples, for 5–15 %Co@$C_{12}E_4$ the TiO_{2-x} that forms is determined to be amorphous, permeable and does not cover the NPs so such an extent; thus it can be considered as decoration to the Co NPs [8]. In contrast, the TiO_{2-x} present on the samples where the surfactant was removed before heating, excessive coverage of the Co NPs was observed, by crystalline and impermeable Ti_2O_3 (See Scheme 1). We note that this phase has not been previously identified. This suggests that there is scope to optimise the interaction between the Co NPs and TiO_2 although there is also a risk that too much TiO_2 migration can be problematic even for the rutile polymorph. Critically, it is the surfactant residue that remains after initial thermal treatment that mitigates the titania reduction and encapsulation[60], although as shown here this can be removed by prolonging reduction time or increasing temperature [13]. We note however that this latter treatment needs to strike a balance between being sufficient to effect surfactant removal whilst not leading to excessive titania reduction/Co NP coverage. This study demonstrated that the conditions used here (e.g. 50 % H_2/He, 623 K, 3 h) is beneficial for producing a more active catalyst although there is likely scope for further optimisation of these conditions. This method is of course not limited to the preparation of Co NPs on TiO_2 and may be translated to the preparation of the same CoNPs on other reducible supports (e.g. Nb_2O_5[10]) else used for the supporting of other metal (Au[13], Rh[58], etc.) NPs thereby expanding the application of surfactant encapsulation to optimise the performance of a catalyst. Catalysts with size-controlled NPs can be easily obtained using this method by simply varying the amount of precursor during NPs preparation. Lastly, the protection of titania reduction by a surfactant can also be applied to some conventional methods for catalyst preparation such as impregnation, for example coating the dried or calcined samples with surfactant (with further heating treatment) before reduction.

4. Methods

4.1. Catalyst preparation

With reference to previously used pentaethylene glycol dodecylether ($C_{12}E_5$),[33] here an affordable tetraethylene glycol monododecyl ($C_{12}E_4$, Brij® L4, Sigma-Aldrich) was chosen as an
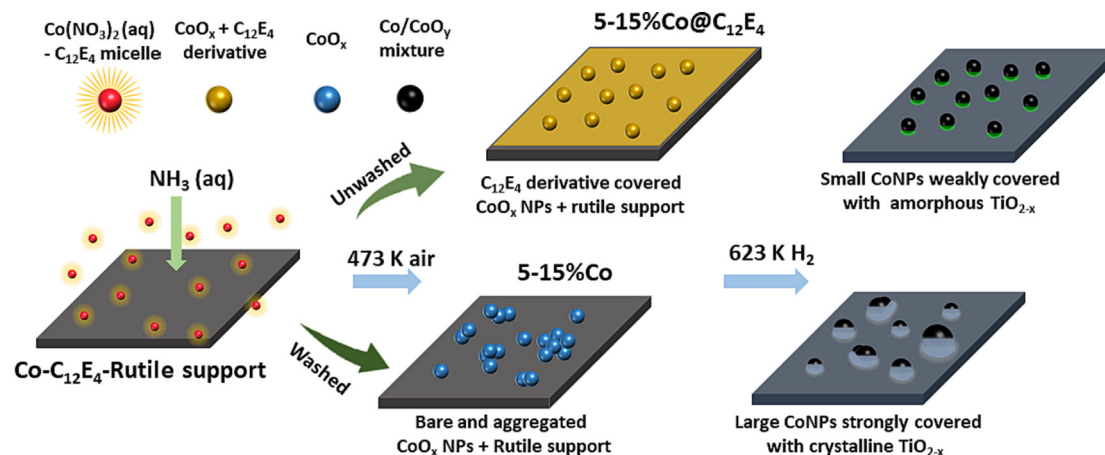
Scheme 1. (Top) Surface $C_{12}E_4$ residues prevent the CoNPs from aggregating and rutile from being reduced. In addition, the gold-coloured sheet in the 473 K calcined 5–15 % Co@$C_{12}E_4$ sample represents the residual $C_{12}E_4$ on the surface, while in the 5–15 %Co sample, the aggregated NPs were shown as blue spheres. TiO$_{2-x}$ migrates in the 5–15 %Co sample and forms a crystalline and impermeable surface (grey solid semicircles), while the partial coverage seen in 5–15 %Co@$C_{12}E_4$ occurs (top depiction) to a lower extent whilst retaining an amorphous and permeable character, (green colour).

alternative surfactant. 5.00 g $C_{12}E_4$ mixing with 26.67 g *n*-hexane (Sigma-Aldrich) were put into a 303 K water bath and stirred at 500 rpm for 2 h to form reverse micelles solution. Then 0.96 g cobalt nitrate hexahydrate (Sigma-Aldrich, > 98 %) in 0.44 g DI water was added and kept stirring for another 1 h under the same conditions. After that, 3.70 g rutile TiO$_2$ (50 m^2/g, Sigma-Aldrich, 6 h 773 K air calcination before use) was added in the above solution and continuing stirring for another 1 h. Then the system was added with 28 wt% NH$_3$ (aq) (0.41 g, Sigma-Aldrich) to generate solid NPs and kept stirring for 1 h. Next, splitting the above green mixture into two portions, one portion was dropwise added with > 80 mL acetone (Sigma-Aldrich) to break micelles. The acquired precipitation and liquid mixture was filtered to remove hexane and $C_{12}E_4$ and then washed for 3–5 times by acetone before drying at 373 K for 12 h and calcining at 473 K for > 5 h [33,63]. The generated catalyst was denoted as 5 %Co. The other portion before calcination was heated to 323 K to evaporate hexane and then the obtained sample was referred to 5 %Co@$C_{12}E_4$. Both cobalt loadings in above catalysts were 5 wt%, but decreasing the amounts of rutile, the 15 wt% cobalt loading catalysts were prepared and denoted as 15 %Co and 15 %Co@$C_{12}E_4$, respectively. Sample reduction, normally, was conducted in a HIDEN CATLAB Microreactor with the condition of 50 % H$_2$/He flow (20 mL/min), 623 K for 3 h. The reduced samples were either passivated by 1 % O$_2$/He (303 K, 50 mL/min, 30 min) or protected in pure ethanol before further characterisation.

4.2. UV–vis

The changes of cobalt nitrate-$C_{12}E_4$ micelles in hexane during adding NH$_3$ (aq) was characterised using a SHIMADZU UV-1800 UV–vis spectrometer in the wavelength range from 300 to 900 nm with a spectral resolution of 2 nm. The measurement conditions were at room temperature and atmosphere and using a pure hexane solvent as reference.

4.3. FTIR

Organic groups residing on above calcined catalysts were studied by FTIR. Before measurement, all the samples were dried at 373 K for 1 h. After cooling down to room temperature, each of the catalysts was diluted with KBr powder, and pressed into 1 mm thick pellets. FTIR measurements were carried out in a

Nicolet iS10 spectrometer under transmission mode with spectral resolution of 4 cm^{-1}.

4.4. TGA

~10 mg sample was analysed in a TGA Q50 V20.13 Build 39 instrument with 50 mL/min N$_2$ flow. Temperature was ramped from room temperature to 1273 K (10 K/min). Specifically, the reduced samples were obtained with the reduction treatment in catalyst preparation (section 1) but without protection during sample transfer. Then first derivative profiles were obtained by processing the TGA (weight loss) profiles with origin Pro 2019.

4.5. TEM/STEM

Before measurement, the samples were reduced using the above mentioned conditions but with an additional passivation process (303 K, 1 % O$_2$/He). Reduced catalysts were quickly dispersed using ethanol and an ultrasonic bath (10 min) and then the supernatant was dropped onto a copper TEM grid (mesh size 200) with a carbon film. Next, the sample was dried in air at room temperature and TEM imaging was conducted using a JEOL JEM2100 TEM 200 kV instrument (RCaH). HAADF-STEM and dual-EELS were performed using a JEOL ARM200CF microscope (ePSIC, Diamond Light Source) operated at 200 kV. FFT patterns and EELS spectra were extracted from exact regions (i.e. region 1 for pure TiO$_2$ support, region 2 for cobalt-TiO$_2$ interface, region 3–7 for different parts of a CoNP and region 8 for background) shown in Fig. 6 and Fig. 7. The TEM/STEM images and FFT patterns were analysed using the ImageJ software (version 1.52e) [64,65]. The NP size is averaged from manually measuring over 100 NPs. The selected EELS spectra were background corrected by using a Gatan DigitalMicrograph software (version 3.30.2016.0) and the EELS references were from EELSDB and EELDC database.

4.6. XRD

A Rigaku Miniflex X-ray diffraction (XRD) instrument (Cu Kα1, 45 kV, 2θ 20–70°, step 0.01°, speed 0.2 s/°) with fixed divergence slits at ISIS neutron and muon light source was used for measurement. The samples were also reduced at 623 K for 3 h in 50 % H$_2$/He flow (20 mL/min) and then cooled down to 303 K but quickly moved into ethanol without passivation. Reduced samples measurement was protected by the ethanol solvent and used a low

noise Si background holder while the calcined samples were a standard XRD run at room temperature. The loading of samples on the pucks is just ensuring the sample is finely ground and has a nice flat surface with respect to the puck edge.

4.7. H_2-TPR

Reducibility of the catalysts was tested by employing an Anton Paar ChemBET Pulsar chemisorption analyzer. The H_2-TPR procedures were: pre-treating catalysts in pure He flow (50 mL/min) at 393 K for 30 min then cooling down to 303 K with changing gas to 10 % H_2/N_2 (50 mL/min) and lastly ramping to 1073 K (10 K/min). The outlet gases were analysed by a Thermal Conductivity Detector (TCD) detector. Particularly, the DOR calculations were conducted at an isothermal temperature step of 623 K for 3 h as part of the experiment. DOR calculations were based on the H_2 consumption ratios at temperatures $\leq$ 623 K versus the total temperature range in the H_2-TPR profiles.

4.8. XPS

XPS analysis for the reduced samples with passivation (same as that for STEM/TEM) was performed on a Thermo Fisher Scientific NEXSA spectrometer at HarwellXPS. This XPS was equipped with a micro-focused monochromatic Al X-ray source (72 W, 400 μm). Data were recorded at pass energies of 50 eV for Co 2p and O 1 s scans with 0.1 eV step size. The samples were measured under the vacuum of 10^{-9} mbar and room temperature with a charge neutralisation mode. The recorded data were analysed by CasaXPS (version 2.3.19PR1.0) [66]. The binding energy was calibrated by using C 1 s (284.8 eV).

4.9. Activity for CO reduction

Ambient pressure CO reduction activity was tested on the HIDEN CATLAB Microreactor. 150 mg powder catalyst was loaded in a quartz tube reactor (using quartz wool to stop catalyst moving) and then reduced in 50 % H_2/He (20 mL/min) at 623 K for 1/3/5 h. After that, the catalyst was cooled down to 423 K and switched to syngas (H_2 3.3 mL/min; 10 % CO/He 16.7 mL/min). Lastly, the temperature was ramped to 493 K and kept for > 1.5 h. The outlet gases before and after reaction were recorded by using an equipped mass spectrometer (MS) with m/e equal to 2, 4, 15, 18, 26, 27, 28, 41, 43, 44, 57, 58, 71. The CO conversions were calculated based on the MS CO calibrated intensity (m/e = 28) changes. Note all the fragments' intensities (i.e. m/e = 2, 15, 18 … 71) were calibrated by the inert standard gas He (m/e = 4).

$$CO conversion = \frac{\frac{I_{CO}}{I_{He}}(initial) - \frac{I_{CO}}{I_{He}}(FTS)}{\frac{I_{CO}}{I_{He}}(initial)} \times 100\%$$

Data availability

Data will be made available on request.

Declaration of Competing Interest

The authors declare that they have no known competing financial interests or personal relationships that could have appeared to influence the work reported in this paper: [Andrew Beale reports a relationship with Finden Ltd that includes: consulting or advisory, employment, equity or stocks, funding grants, non-financial support, and travel reimbursement].

Appendix A. Supplementary material

Supplementary data to this article can be found online at https://doi.org/10.1016/j.jcat.2023.02.002.

References

[1] S. Storsæter, B. Tøtdal, J.C. Walmsley, B.S. Tanem, A. Holmen, Characterization of alumina-, silica-, and titania-supported cobalt fischer-tropsch catalysts, J. Catal. 236 (1) (2005) 139–152.
[2] M.K. Gnanamani, M.C. Ribeiro, W. Ma, W.D. Shafer, G. Jacobs, U.M. Graham, B. H. Davis, Fischer-tropsch synthesis: metal-support interfacial contact governs oxygenates selectivity over CeO$_2$ supported Pt-Co catalysts, Appl. Catal. A Gen. 393 (1–2) (2011) 17–23.
[3] C. Xing, G. Yang, M. Wu, R. Yang, L. Tan, P. Zhu, Q. Wei, J. Li, J. Mao, Y. Yoneyama, N. Tsubaki, hierarchical zeolite y supported cobalt bifunctional catalyst for facilely tuning the product distribution of fischer-tropsch synthesis, Fuel 148 (2015) 48–57.
[4] A. Karimi, B. Nasernejad, A.M. Rashidi, A. Tavasoli, M. Pourkhalil, Functional group effect on carbon nanotube (CNT)-Supported Cobalt catalysts in fischer-tropsch synthesis activity, Selectivity and Stability. *Fuel* 117 (2014) 1045–1051.
[5] Y. Liu, B. De Tymowski, F. Vigneron, I. Florea, O. Ersen, C. Meny, P. Nguyen, C. Pham, F. Luck, C. Pham-Huu, Titania-decorated silicon carbide-containing cobalt catalyst for fischer-tropsch synthesis, ACS Catal. 3 (3) (2013) 393–404.
[6] J.H. Oh, J.W. Bae, S.J. Park, P.K. Khanna, K.W. Jun, Slurry-Phase Fischer-Tropsch Synthesis Using Co/γ-Al$_2$O$_3$, Co/SiO$_2$ and Co/TiO$_2$: effect of support on catalyst aggregation, Catal. Lett. 130 (3–4) (2009) 403–409.
[7] M. Voß, D. Borgmann, G. Wedler, Characterization of Alumina, Silica, and Titania Supported Cobalt Catalysts, J. Catal. 212 (1) (2002) 10–21.
[8] V. A. de la Peña O'Shea, M. Consuelo Álvarez Galván, A. E. Platero Prats, J. M. Campos-Martin, J. L. G. Fierro, Direct Evidence of the SMSI Decoration Effect: the Case of Co/TiO$_2$ Catalyst. *Chem. Commun.* **2011**, *47* 25, 7131.
[9] C.E. Kliewer, S.L. Soled, G. Kiss, Morphological transformations during fischer-tropsch synthesis on a titania-supported cobalt catalyst, Catal. Today 323 (2019) 233–256.
[10] C. Hernández Mejía, T.W. van Deelen, K.P. de Jong, Activity enhancement of cobalt catalysts by tuning metal-support interactions, Nat. Commun. 9 (1) (2018) 1–8.
[11] G. Melaet, W.T. Ralston, C.S. Li, S. Alayoglu, K. An, N. Musselwhite, B. Kalkan, G. A. Somorjai, Evidence of Highly Active Cobalt Oxide Catalyst for the Fischer-Tropsch Synthesis and CO$_2$ Hydrogenation, J. Am. Chem. Soc. 136 (6) (2014) 2260–2263.
[12] T.W. van Deelen, C. Hernández Mejía, K.P. de Jong, Control of metal-support interactions in heterogeneous catalysts to enhance activity and selectivity, Nat. Catal. 2 (11) (2019) 955–970.
[13] H. Tang, Y. Su, B. Zhang, A.F. Lee, M.A. Isaacs, K. Wilson, L. Li, Y. Ren, J. Huang, M. Haruta, B. Qiao, X. Liu, C. Jin, D. Su, J. Wang, T. Zhang, Classical strong metal-support interactions between gold nanoparticles and titanium dioxide, Sci. Adv. 3 (10) (2017) 1–9.
[14] F. Bertella, P. Concepción, A. Martínez, TiO$_2$ Polymorph Dependent SMSI Effect in Co-Ru/TiO$_2$ catalysts and its relevance to fischer-tropsch synthesis, Catal. Today 289 (2017) 181–191.
[15] B. Jongsomjit, C. Sakdamnuson, J.G. Goodwin, P. Praserthdam, Co-support compound formation in titania-supported cobalt catalyst, Catal. Lett. 94 (3–4) (2004) 209–215.
[16] F. Pacheco, M. Gonzalez, A. Medina, S. Velumani, J.A. Ascencio, Structural analysis of cobalt titanate nanoparticles obtained by sol-gel process, Appl. Phys. A Mater. Sci. Process. 78 (4) (2004) 531–536.
[17] M. Wolf, E.K. Gibson, E.J. Olivier, J.H. Neethling, C.R.A. Catlow, N. Fischer, M. Claeys, Water-induced formation of cobalt-support compounds under simulated high conversion fischer-tropsch environment, ACS Catal. 9 (2019) 4902–4918.

[18] C. Qiu, Y. Odarchenko, Q. Meng, P. Cong, M.A.W. Schoen, A. Kleibert, T. Forrest, A.M. Beale, Direct observation of the evolving metal-support interaction of individual cobalt nanoparticles at the titania and silica interface, Chem. Sci. 11 (48) (2020) 13060–13070.

[19] K.H. Cats, J.C. Andrews, O. Stéphan, K. March, C. Karunakaran, F. Meirer, F.M.F. De Groot, B.M. Weckhuysen, Active phase distribution changes within a catalyst particle during fischer-tropsch synthesis as revealed by multi-scale microscopy, Catal. Sci. Technol. 6 (12) (2016) 4438–4449.

[20] T.W. Van Deelen, J.J. Nijhuis, N.A. Krans, J. Zečević, K.P. De Jong, Preparation of cobalt nanocrystals supported on metal oxides to study particle growth in fischer-tropsch catalysts, ACS Catal. 8 (11) (2018) 10581–10589.

[21] T.O. Eschemann, J. Oenema, K.P. De Jong, Effects of Noble Metal Promotion for Co/TiO$_2$ Fischer-Tropsch Catalysts, Catal. Today 261 (2016) 60–66.

[22] J. Hong, B. Wang, G. Xiao, N. Wang, Y. Zhang, A.Y. Khodakov, J. Li, Tuning the metal-support interaction and enhancing the stability of titania-supported cobalt fischer-tropsch catalysts via carbon nitride coating, ACS Catal. 10 (10) (2020) 5554–5566.

[23] T.N. Phaahlamohlaka, M.W. Dlamini, M.W. Mogodi, D.O. Kumi, L.L. Jewell, D.G. Billing, N.J. Coville, A sinter resistant co fischer-tropsch catalyst promoted with Ru and supported on titania encapsulated by mesoporous silica, Appl. Catal. A Gen. 552 (2018) 129–137.

[24] G.L. Bezemer, J.H. Bitter, H.P.C.E. Kuipers, H. Oosterbeek, J.E. Holewijn, X. Xu, F. Kapteijn, A.J. Van Diilen, K.P. De Jong, Cobalt particle size effects in the fischer-tropsch reaction studied with carbon nanofiber supported catalysts, J. Am. Chem. Soc. 128 (12) (2006) 3956–3964.

[25] P. Van Helden, I.M. Ciobîca, R.L.J. Coetzer, The size-dependent site composition of FCC Cobalt Nanocrystals, Catal. Today 261 (2016) 48–59.

[26] J.P. den Breejen, P.B. Radstake, G.L. Bezemer, J.H. Bitter, V. Frøseth, A. Holmen, K.P. de Jong, On the origin of the cobalt particle size effects in fischer–tropsch catalysis, J. Am. Chem. Soc. 131 (20) (2009) 7197–7203.

[27] J.X. Liu, P. Wang, W. Xu, E.J.M. Hensen, Particle size and crystal phase effects in fischer-tropsch catalysts, Engineering 3 (4) (2017) 467–476.

[28] B. Zeng, B. Hou, L. Jia, J. Wang, C. Chen, Y. Sun, D. Li, Studies of Cobalt Particle Size Effects on Fischer-Tropsch Synthesis over Core-Shell-Structured Catalysts, ChemCatChem. 5 (12) (2013) 3794–3801.

[29] Y. Dai, Y. Zhao, T. Lin, S. Li, F. Yu, Y. An, X. Wang, K. Xiao, F. Sun, Z. Jiang, Y. Lu, H. Wang, L. Zhong, Y. Sun, Particle size effects of cobalt carbide for fischer-tropsch to olefins, ACS Catal. 9 (2) (2019) 798–809.

[30] P. Ghasvareh, K.J. Smith, Effects of Co Particle Size on the Stability of Co/Al$_2$O$_3$ and Re-Co/Al$_2$O$_3$ Catalysts in a Slurry-Phase Fischer-Tropsch Reactor, Energy and Fuels 30 (11) (2016) 9721–9729.

[31] M. Wolf, H. Kotzé, N. Fischer, M. Claeys, Size dependent stability of cobalt nanoparticles on silica under high conversion fischer-tropsch environment, Faraday Discuss. 197 (2017) 243–268.

[32] R. Agrawal, P. Phatak, L. Spanu, Effect of phase and size on surface sites in cobalt nanoparticles, Catal. Today 312 (2018) 174–180.

[33] N. Fischer, E. Van Steen, M. Claeys, Preparation of supported nano-sized cobalt oxide and Fcc Cobalt Crystallites, Catal. Today 171 (1) (2011) 174–179.

[34] V.F. Puntes, K.M. Krishnan, P.A. Alivisatos, colloidal nanocrystal shape and size control : the case of cobalt, Science. 291 (5511) (2001) 2115–2117.

[35] A. Martínez, G. Prieto, Breaking the dispersion-reducibility dependence in oxide-supported cobalt nanoparticles, J. Catal. 245 (2) (2007) 470–476.

[36] S. Sun, C.B. Murray, Synthesis of monodisperse cobalt nanocrystals and their assembly into magnetic superlattices, J. Appl. Phys. 85 (1999) 4325–4330.

[37] Ø. Borg, P.D.C. Dietzel, A.I. Spjelkavik, E.Z. Tveten, J.C. Walmsley, S. Diplas, S. Eri, A. Holmen, E. Rytter, Fischer-tropsch synthesis: cobalt particle size and support effects on intrinsic activity and product distribution, J. Catal. 259 (2) (2008) 161–164.

[38] K. Cheng, V. Subramanian, A. Carvalho, V.V. Ordomsky, Y. Wang, A.Y. Khodakov, The role of carbon pre-coating for the synthesis of highly efficient cobalt catalysts for fischer-tropsch synthesis, J. Catal. 337 (2016) 260–271.

[39] W. Zhan, Q. He, X. Liu, Y. Guo, Y. Wang, L. Wang, Y. Guo, A.Y. Borisevich, J. Zhang, G. Lu, S. Dai, A sacrificial coating strategy toward enhancement of metal-support interaction for ultrastable Au nanocatalysts, J. Am. Chem. Soc. 138 (49) (2016) 16130–16139.

[40] W. Zhan, Y. Shu, Y. Sheng, H. Zhu, Y. Guo, L. Wang, Y. Guo, J. Zhang, G. Lu, S. Dai, Surfactant-Assisted Stabilization of Au Colloids on Solids for Heterogeneous Catalysis, Angew. Chemie - Int. Ed. 56 (16) (2017) 4494–4498.

[41] J.P. Spatz, S. Mössmer, C. Hartmann, M. Möller, T. Herzog, M. Krieger, H.G. Boyen, P. Ziemann, B. Kabius, Ordered deposition of inorganic clusters from micellar block copolymer films, Langmuir 16 (2) (2000) 407–415.

[42] U. Wiedwald, L. Han, J. Biskupek, U. Kaiser, P. Ziemann, Preparation and characterization of supported magnetic nanoparticles prepared by reverse micelles, Beilstein J. Nanotechnol. 1 (1) (2010) 24–47.

[43] H.G. Boyen, G. Kästle, K. Zürn, T. Herzog, F. Weigl, P. Ziemann, O. Mayer, C. Jerome, M. Möller, J.P. Spatz, M.G. Garnier, P. Oelhafen, A Micellar route to ordered arrays of magnetic nanoparticles: from size-selected pure cobalt dots to cobalt-cobalt oxide core-shell systems, Adv. Funct. Mater. 13 (5) (2003) 359–364.

[44] J.W. Wang, Y.M. Kuo, Synthesis of nanosized zinc-doped cobalt oxyhydroxide parties by a dropping method and their carbon monoxide gas sensing properties, J. Nanomater. (2013).

[45] A. Dwivedi, B.K. Sharma, N. Rajagopalan, S. Sinha, Hydrothermal decomposition of cobalt hydroxide in saturated water vapor, Ind. Eng. Chem. Res. 59 (1) (2020) 491–496.

[46] N. Koizumi, S. Suzuki, S. Niiyama, Y. Ibi, T. Shindo, M. Yamada, Effects of glycols on fischer-tropsch synthesis activity and coordination Structure of Co Species in Co/SiO$_2$: mechanism for enhanced dispersion of Co^0 Nanoparticles, Appl. Catal. A Gen. 395 (1–2) (2011) 138–145.

[47] B. Xiao, W. Zhu, Z. Li, J. Zhu, X. Zhu, G. Pezzotti, Tailoring morphology of cobalt - nickel layered double hydroxide via different surfactants for high-performance supercapacitor, R. Soc. Open Sci. 5 (2018).

[48] R. Riva, H. Miessner, R. Vitali, G. Del Piero, Metal-Support Interaction in Co/ SiO$_2$ and Co/TiO$_2$, Appl. Catal. A Gen. 196 (1) (2000) 111–123.

[49] Z. Liu, B. Ge, K. Li, X. Zhang, K. Huang, The excellent performance and mechanism of activated carbon air cathode doped with different type of cobalt for microbial fuel cells, Fuel 176 (2016) 173–180.

[50] B.A. Sexton, A.E. Hughes, T.W. Turney, An XPS and TPR Study of the reduction of promoted cobalt-kieselguhr fischer-tropsch catalysts, J. Catal. 97 (2) (1986) 390–406.

[51] Y. Zhang, D. Wei, S. Hammache, J.G. Goodwin, Effect of Water Vapor on the Reduction of Ru-Promoted Co/Al$_2$O$_3$, J. Catal. 188 (2) (1999) 281–290.

[52] D.S. Kim, Y.H. Kim, J.E. Yie, E.D. Park, The effect of cobalt precursors on NO oxidation over supported cobalt oxide catalysts, Korean J. Chem. Eng. 27 (3) (2010) 822–827.

[53] K. Joseph Antony Raj, M. G. Prakash, T. Elangovan, B. Viswanathan, Selective Hydrogenation of Cinnamaldehyde over Cobalt Supported on Alumina, Silica and Titania. *Catal. Letters* **2012**, *142* 1 87–94.

[54] K. Rahbar Shamskar, A. Rashidi, P. Aberoomand Azar, M. Yousefi, S. Baniyaghoob, Synthesis of Graphene by in Situ Catalytic Chemical Vapor Deposition of Reed as a Carbon Source for VOC Adsorption. *Environ. Sci. Pollut. Res.* **2019**, *26* 4 3643–3650. (55) Lancelot, C.; Ordomsky, V. V.; Stéphan, O.; Sadeqzadeh, M.; Karaca, H.; Lacroix, M.; Curulla-Ferré, D.; Luck, F.; Fongarland, P.; Griboval-Constant, A.; Khodakov, A. Y. Direct Evidence of Surface Oxidation of Cobalt Nanoparticles in Alumina-Supported Catalysts for Fischer-Tropsch Synthesis. *ACS Catal.* **2014**, *4* (12), 4510–4515.

[55] A.R. Puigdollers, P. Schlexer, S. Tosoni, G. Pacchioni, Increasing Oxide Reducibility: the role of Metal/Oxide interfaces in the formation of oxygen vacancies, ACS Catal. 7 (10) (2017) 6493–6513.

[56] Q. Fu, T. Wagner, Interaction of Nanostructured Metal Overlayers with Oxide Surfaces, Surface Sci. Rep. 431–498 (2007).

[57] J.C. Matsubu, S. Zhang, L. DeRita, N.S. Marinkovic, J.G. Chen, G.W. Graham, X. Pan, P. Christopher, Adsorbate-mediated strong metal-support interactions in oxide-supported Rh catalysts, Nat. Chem. 9 (2) (2017) 120–127.

[58] H. Li, X. Weng, Z. Tang, H. Zhang, D. Ding, M. Chen, H. Wan, Evidence of the encapsulation model for strong metal-support interaction under oxidized conditions: a case study on TiO$_x$/Pt(111) for CO oxidation by in situ wide spectral range infrared reflection adsorption spectroscopy, ACS Catal. 8 (11) (2018) 10156–10163.

[59] S. Liu, W. Xu, Y. Niu, B. Zhang, L. Zheng, W. Liu, L. Li, J. Wang, Ultrastable Au nanoparticles on titania through an encapsulation strategy under oxidative atmosphere, Nat. Commun. 10 (1) (2019) 1–9.

[60] S.J. Tauster, S.C. Fung, R.T.K. Baker, J.A. Horsley, Strong interactions in supported-metal catalysts, Science. 211 (4487) (1981) 1121–1125.

[61] S.J. Tauster, Strong metal-support interactions, Acc. Chem. Res. 20 (11) (1987) 389–394.

[62] N. Fischer, T. Feltes, M. Claeys, CRC concise encyclopedia of nanotechnology, CRC Press, 2016.

[63] X. Liu, M. Atwater, J. Wang, Q. Huo, Extinction coefficient of gold nanoparticles with different sizes and different capping ligands, Colloids Surf. B Biointerfaces 58 (1) (2007) 3–7.

[64] V. Prathibha, S. Karthika, J. Cyriac, C. Sudarasanakumar, N.V. Unnikrishnan, Synthesis of Pure Anatase TiO$_2$ Nanocrystals in SiO$_2$ host and the determination of crystal planes by image, J. *Mater. Lett.* 65 (4) (2011) 664–666.

[65] M.C. Biesinger, B.P. Payne, A.P. Grosvenor, L.W.M. Lau, A.R. Gerson, R.S.C. Smart, Resolving surface chemical states in XPS analysis of first row transition metals, oxides and hydroxides: Cr, Mn, Fe, Co and Ni. *Appl. Surf. Sci.* 257 (7) (2011) 2717–2730.